Optomechanical Modulation Spectroscopy of Bound States in the Continuum in a Dielectric Metasurface

S. Zanotto,[1,†] G. Conte ®,[1,2,†] L. C. Bellieres,[3] A. Griol,[3] Daniel Navarro-Urrios,[4] A. Tredicucci ®,[1,2]
A. Martínez ®,[3] and A. Pitanti ®[1,*]

[1]*NEST Lab., CNR—Istituto di Nanoscienze and Scuola Normale Superiore, Piazza San Silvestro 12, Pisa 56217, Italy*
[2]*Dipartimento di Fisica, Università di Pisa, Largo Pontecorvo 3, Pisa 56127, Italy*
[3]*Nanophotonics Technology Center, Universitat Politècnica de Valencia, Spain*
[4]*MIND-IN2UB, Departament d'Electrònica, Facultat de Física, Universitat de Barcelona, Martí i Franquès 1, Barcelona 08028, Spain*

Elusive features in photonic and electronic devices can be detected by means of advanced, time-domain spectroscopic techniques. In this paper we introduce a modulation spectroscopy based on the optomechanical interaction of photonic and mechanical modes. Applying the technique to a Si metasurface and its drumlike mechanical modes, we detect narrow-band quasi-bound-state-in-the-continuum (quasi-BIC) modes close to normal incidence, where their measurement can be hindered by a high-symmetry protection and undesired background modes. Showing a visibility enhancement of more than one order of magnitude, the optomechanical modulation spectroscopy can be an innovative tool for precise spectroscopy of a wide set of photonic devices, including the goal of measuring purely symmetry protected BIC resonances.

I. INTRODUCTION

Spectroscopic techniques are extremely powerful tools to investigate the properties of a wide set of materials and devices using almost noninvasive light probes [1]. Classical spectroscopy, where reflectivity and transmissivity of a test sample are investigated using tunable or broad-band continuous-wave (cw) sources, have been quickly sided by more complex techniques exploiting dynamical effects. Modulation-based spectroscopy can comprise either an *external* modulation of the energy of the impinging monochromatic source (wavelength modulation spectroscopy) [2,3] or an *inner* modulation of the sample properties. The latter approach manifests in many techniques, including excitation-modulation spectroscopy, photoreflectance or pump-probe techniques in semiconductors [4,5]; classic schemes have found a recent application in investigation of optical plasmons [6] and two-dimensional materials [7]. Notably, a pure *inner* modulation spectroscopy using single cw optical sources requires particular device characteristics: so far, it essentially included the possibility of charge density tuning (charged modulation spectroscopy) in optoelectronic devices based on organic semiconductors [8] and

field-effect transistors [9]. Both *outer* and *inner* modulation techniques are based on the idea that the derivative of a weak signal can be used for peak detection [10] and for enhancing its visibility by background removal, within a scheme sometimes labeled derivative spectroscopy [11].

In this paper, we introduce a *purely inner* spectroscopy technique, which we term optomechanical modulation spectroscopy (OMS), based on optomechanical modulation of photonic device features. Optomechanics has recently risen as a research avenue where the coupling of photons with the ubiquitous mechanical modes has been investigated in several different kinds of devices [12]. The foremost concept in this field is the possibility of modulating light through mechanical action, via a complex coefficient that governs dispersive and/or dissipative coupling. Remarkably, thermally excited modes can modulate an incident optical wave without the need for generating external actuation. We anticipate that OMS can be used to selectively enhance photonic features in multiresonance systems and can be implemented in all samples featuring mechanical action, which is diffusely present in photonic devices. For example, it can have an interest for photonic crystals, metasurfaces, whispering gallery mode resonators on top of substrates, as well as for fiber-coupled waveguide systems with undesired fiber-facet multiple reflection. Here, we exploit the optomechanical modulation for enhancing spectroscopic features: the potential of

———————
*alessandro.pitanti@nano.cnr.it
†First two authors contributed equally.

044033-1

OMS is shown by characterizing photonic bound states in the continuum (BIC) in a Si metasurface. BICs are a general wave phenomenon where the states, despite having an energy within the radiative continuum, are interference or symmetry protected from leaking out to the external world. Being initially proposed in quantum mechanics [13], experimental and theoretical investigations of BICs has lately extended to several wave systems [14], with a special focus on photonics, both in waveguide arrays [15,16] and planar systems [17–19]. Pure BICs have infinite radiative Q factors and are therefore invisible to external probes. The symmetry conditions necessary for a pure BIC can be fulfilled considering precise points in the system phase space; most commonly, BICs are found around Γ points, yet in some cases accidental symmetry conditions could be realized in different points of the reciprocal space. Small deviations from the perfect symmetry protection couples the state with the continuum, giving it a finite radiative Q factor and granting the possibility of accessing it from outside (quasi-BIC). BICs and quasi-BICs have been subjected to a wide investigation, in the context of fundamental physics and topology [20,21] as well as for applications, offering ultrahigh Q factors in delocalized photonic devices such as metasurfaces. This allows exploiting far-field probing, granting several advantages to other ultrahigh Q photonic systems that need near-field coupling [22–24].

To understand the principle of OMS, we start by considering the optomechanical coupling g_{OM} [12], defined as

$$g_{\mathrm{OM}} = \frac{\partial \omega_0}{\partial x}, \qquad (1)$$

where ω_0 is the resonant frequency of a photonic mode and x a generalized mechanical displacement. When a displacement Δx is applied through mechanical motion, the static linear response optical signal from a resonant device, $O_0(\omega)$, gains an extra modulation term, $O(\omega) = O_0(\omega) + M(\omega)\Delta x$, where

$$M(\omega) = \frac{\partial O(\omega)}{\partial x} = -\frac{\partial O(\omega)}{\partial \omega}\frac{\partial \omega_0}{\partial x} = -O'(\omega)g_{\mathrm{OM}}; \quad (2)$$

more details can be found in Appendix A. On the right-hand side of Eq. (2), we get the first derivative of the optical signal; upon integration, we can then use the modulated signal to reconstruct the original optical signal, rescaled by the optomechanical coupling, $O_r(\omega)$. When several resonances are involved, we can use this technique to rescale each of them according to their own g_{OM}. Figure 1 summarizes the main concept behind this idea. Let us suppose that we have the optical feature of interest buried in a wide background [panel (a)]. This feature could be a mode localized in a photonic structure, while the background could be coming from an underlying substrate. Moreover, let us suppose that the two contributions

have different optomechanical couplings, the former possibly being larger than the latter, as routinely found in many photonic devices. Actuating a proper mechanical mode, the modulated signals can be evaluated [panel (b)], leading to a reconstructed signal [panel (c)], where the relative amplitude of the different features has been rescaled according to the ratio of their own optomechanical couplings, resulting in a strongly enhanced feature visibility of an elusive feature.

II. EXPERIMENTAL RESULTS

The BICs investigated with OMS have been implemented relying on a 220 nm Si slab perforated with a square lattice of circular holes; more details on the design are given in Appendix B The device layer, originally on top of sacrificial SiO_2, has been suspended, to maintain a local mirror symmetry along the vertical direction, leaving a 2 μm air layer between it and a thick Si wafer handle; see Fig. 1(d). A SEM micrograph of a fabricated device along with a sketch of its unit cell are shown in Fig. 1(e). More details on device fabrication can be found in Appendix C.
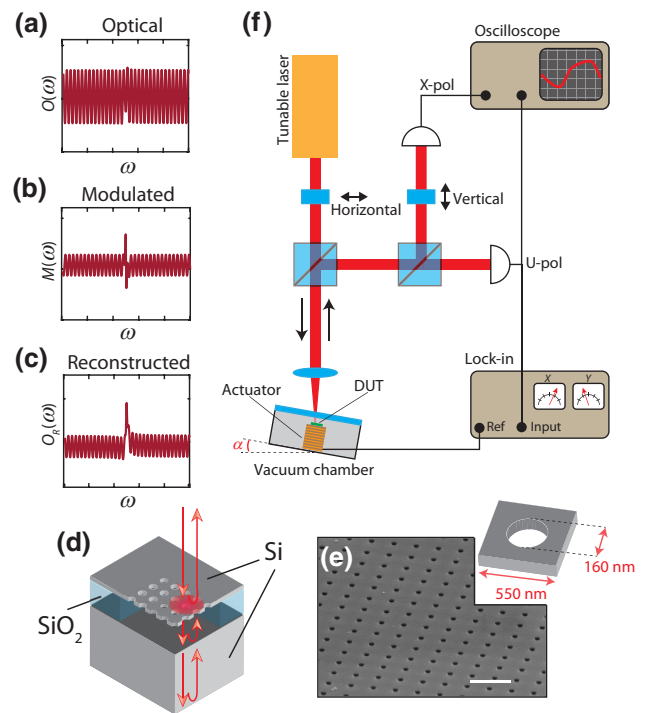

FIG. 1. OMS concept. Hidden features in the optical spectrum (a) are enhanced via the mechanically modulated signal (b), leading to the reconstructed optical signal (c). (d) Case study of a Si metasurface suspended on a Si handle, combining metasurface modes and multiple reflections within the substrate and air layer. (e) SEM micrograph of a fabricated device and sketch of the unit cell. White scale bar is 5 μm. (f) Sketch of the experimental setup for angle-resolved OMS.

Devices under test have been characterized using an angle-resolved reflectivity setup sketched in Fig. 1(f). The setup is comprised a tunable laser source (NewportVe-locity TLB6700) whose 30 mW beam impinges on the device under test (DUT) placed within a vacuum chamber on a motorized stage and with variable tilting α. The filtered or unfiltered reflected signal intensity can be directly measured by means of an InGaAs photodiode (Newport 1623) using an oscilloscope (TekTronix MDO3104) or can be demodulated by a lock-in amplifier (Zurich UHF). Additionally, a $f = 6$ cm lens is used for beam focusing, while few optical components are needed to route the laser beam and manage its polarization state. Unfiltered reflectivity data upon horizontally polarized laser illumination at normal incidence are shown in Fig. 2(a) (U-pol). Here the signal is dominated by multiple reflections originating mostly from the substrate, appearing as narrowly spaced intensity oscillations [see panel (b)]. The average reflectivity is modified by the presence of the SiO_2 sacrificial layer; this can be used to spatially map the region where the metasurface has been defined. The figure inset shows a map of the average signal intensity, where the 75 μm side metasurface can be clearly recognized. In this experimental configuration, the contribution from the metasurface modes is completely hidden and can be partially recovered only by filtering the reflected light using a linear polarizer with axis aligned to the vertical direction. The use of crosspolarized signals [X-pol; see Fig. 2(a)] has been previously used in experiments involving photonic crystals with certain symmetries [25,26]; in our case, the X-pol component originates, at normal incidence, from imperfections in the metasurface pattern (hole circularity, etc.) as well as local membrane bending. Since the polarization rotation power is weaker or absent in the device substrate, the X-pol measurement could be used for enhancing the metasurface modes, as shown in the enlarged view of Fig. 2(c). As a drawback, the X-pol signal is spatially inhomogeneous, since it depends on the local membrane structure. For example, the X-pol peak-to-peak map [inset of Fig. 2(a)] shows large values upon a metasurface corner, while being weaker on the opposite one. This fact, together with the different sensitivities of different modes to local inhomogeneities and their weak intensity, makes the use of X-pol spectra not always reliable for optical spectroscopy. In Appendix D an extensive analysis of the X-pol spectra is reported.

OMS can be introduced by exciting membrane mechanical modes; this is done by placing the device on a piezoelectric piezoceramic multilayer actuator and operating in mild vacuum (about 10^{-3} mbar). Decreasing the thin-film damping, few membrane mechanical modes can be detected by demodulating the polarization-unfiltered light [27] reflected from the device with the ac bias fed to the piezo using the lock-in amplifier [see Fig. 1(f)] [28]. The mechanical mode that we select is shown in
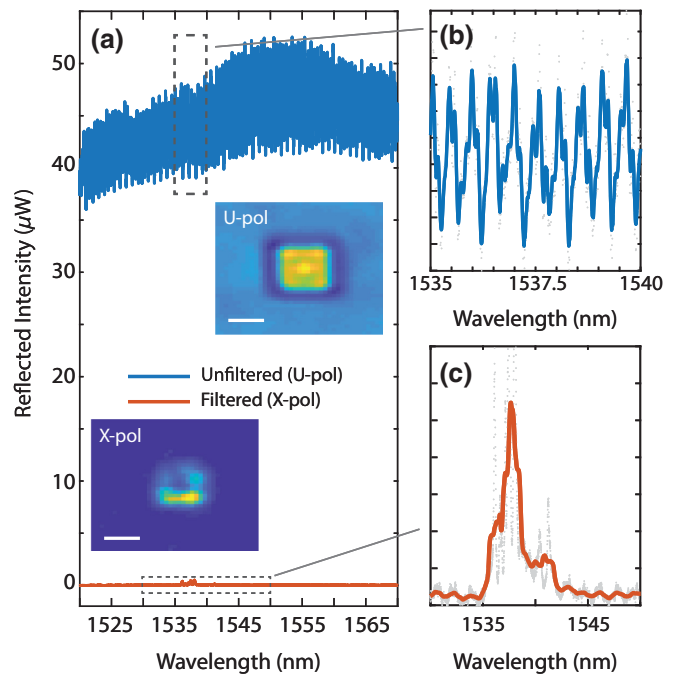

FIG. 2. Polarization dependent reflectivity response. (a) Unfiltered polarization (U-pol) and crosspolarization filtered (X-pol) reflectivity signals from the device. An enlarged view of the two spectra are shown in (b) and (c), respectively. In the inset the maps of the average reflected intensity for U-pol and of the peak-to-peak reflected intensity for X-pol are shown.

Fig. 3(a); this was chosen since it is well separated from the strongest resonance frequencies intrinsic to the piezo actuator (see Appendix C). Note that OMS does not directly depend on the nature of the mechanical mode employed as long as it gives a stronger coupling with the mode of interest with respect to the undesired ones, which is a common configuration when localized and delocalized resonances are considered. The mechanical feature is composed by two peaks, holding Q factors of about 100 and 1500, respectively, limited by molecular damping [28–30]. The finite-element method (FEM) simulated modal shape attributed to both modes has been reported in the same figure. These simulations have shown a large degree of reliability when used in different photonic devices implemented in the same material platform [31]. Feeding the piezo with an ac tone at a frequency of 1.557 MHz, corresponding to the maximum of the mode-(ii) peak, we sweep the laser wavelength and record the reflected and the demodulated intensity (O and M, respectively). Figure 3(b) reports the U-pol and X-pol optical spectra, the latter having been rescaled for visibility. A single narrow feature can be identified only in the X-pol spectra, whereas the modulation amplitude, M, clearly shows two narrow features, one around 1528 nm (mode 1) and the other around 1537 nm (mode 2), respectively; see Fig. 3(c). The reconstructed
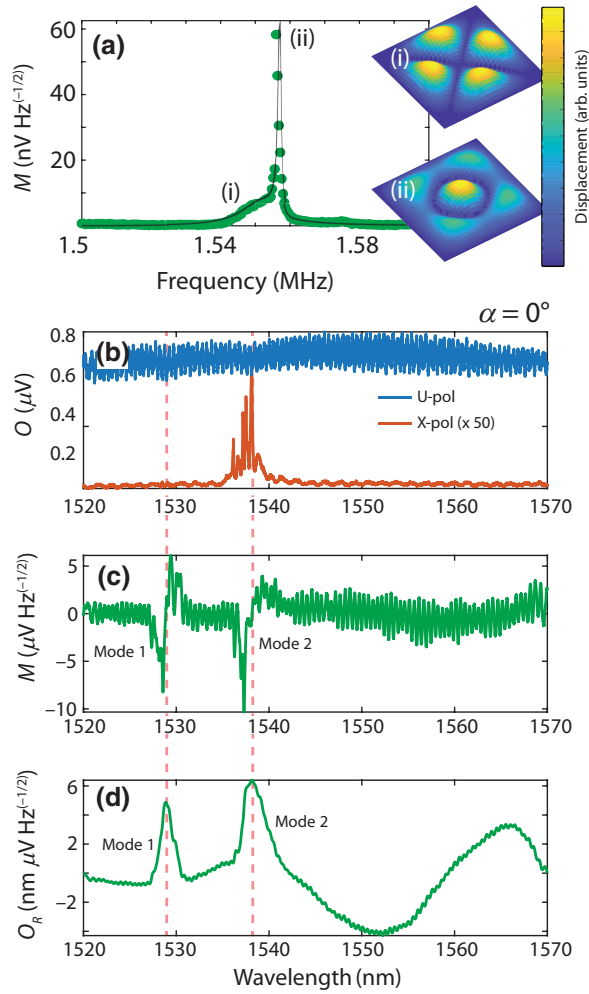
FIG. 3. Shaking the quasi-BIC. (a) Mechanical mode used for OMS. (b) Optical U-pol and X-pol spectra around normal incidence. (c) Demodulated modulation intensity. (d) Reconstructed signal. The dashed pink lines indicate the spectral position of the quasi-BICs under investigation.
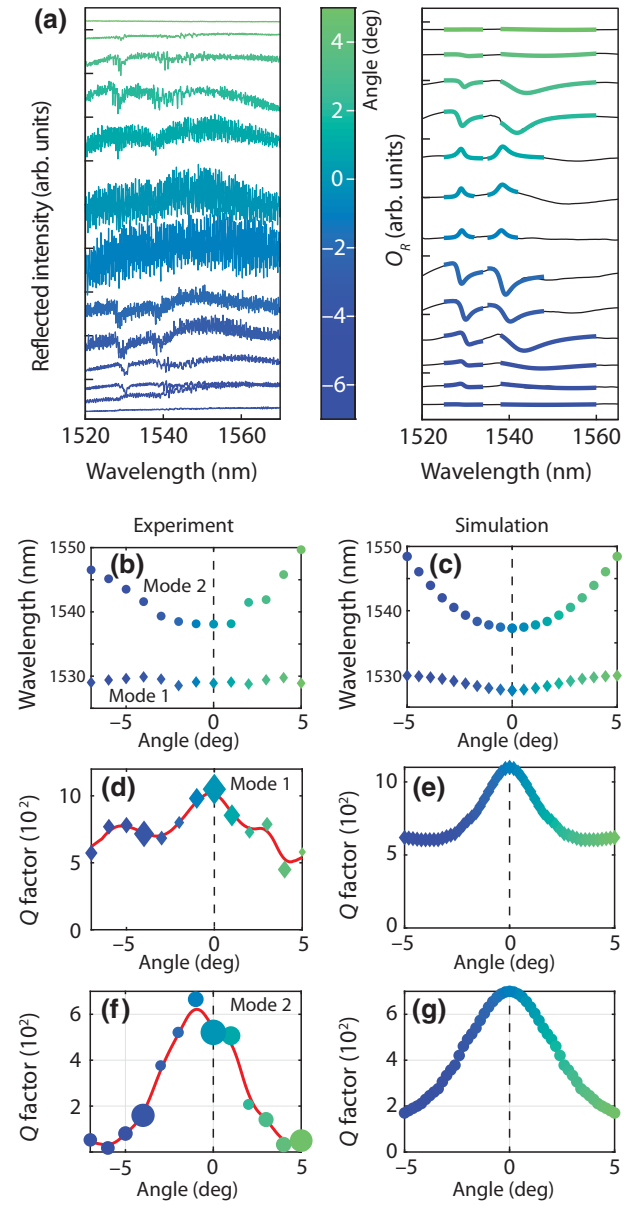

FIG. 4. Quasi-BIC spectroscopy. (a) Waterfall plot of U-pol (left) and reconstructed (right) spectra at the metasurface center for different incident angles. Best fits with Fano lineshapes are indicated with bold, colored lines. (b),(c) Experimental and simulated frequency dispersion. Experimental (d),(f) and simulated Q factors (e),(g) for mode 1 and mode 2, respectively.

optical signal, shown in panel (d), now has two clear resonant features, with a large enhancement in the visibility with respect to the original U-pol reflectivity data. Interestingly, using OMS, we detect two resonant peaks within the laser wavelength range, one of which is completely absent even in the X-pol spectrum. The different X-pol intensity of the two modes is linked to their different sensitivity to imperfections: the electromagnetic field of mode 1 is less confined around the circular metasurface hole than mode 2, the latter being more affected by symmetry breaking involving the hole circularity or surface roughness. Inspecting Eq. (2), we expect the mode enhancement to be proportional to each mode g_{OM}. Using rigorous coupled wave method based simulations [32], we find, at almost normal incidence and in the membrane center, a $g^s_{OM} = 2.99$ kHz optomechanical coupling for the substrate modes and $g^{m1}_{OM} = 51.05$ kHz and $g^{m2}_{OM} = 74.4$ kHz for modes 1

and 2, respectively. These are compatible with the contrast enhancement in Fig. 3(c), with relative increases of factors of about 17 and 25 for mode 1 and mode 2, respectively. More details on the simulations can be found in Appendix B.

To show the power of OMS in the investigation of BICs, we perform standard and optomechanical modulation spectroscopy of the device at different angles of incidence α, illuminating the device in the center of the

metasurface. Figure 4 reports the main results where different spectra have been vertically shifted for clarity [33] and the angle of incidence color coded from blue to green. In the U-pol spectra (leftmost panel) the two quasi-BIC features are visible at large angles, while they are completely hidden by the substrate contribution around normal incidence. This contrast difference can be expected from a simple model based on coupled-mode theory for resonances with varying radiative loss and a constant, small nonradiative loss contribution [34]; detailed considerations can be found in Appendix B. Even if using tilted U-pol spectroscopy for identifying quasi-BICs at finite angles, its performance degrades when getting closer to normal incidence, which is the region with the most detrimental substrate effect yet, but, conversely, the most interesting one since the quasi-BICs tends to the pure BIC modes. A very different situation can be found for the reconstructed signals in the rightmost panel: both quasi-BICs can be identified with a large signal-to-background ratio at every angle, with a generally improved visibility over the U-pol measurement. All the reconstructed signals have been fitted by employing Fano functions, which are naturally used in situations where multiple resonances with different linewidths are coupled together [35,36]. Figure 4(b) shows the extracted resonant wavelength for mode 1 and mode 2 (diamonds and circles, respectively). As can be seen, mode 1 has an almost flat dispersion in the investigated region, whereas mode 2 has a parabolic one. The resonant wavelengths are in very good agreement with FEM simulations for the infinite photonic crystal, which are reported in Fig. 4(c). In quasi-BIC, it is expected that the optical Q factors degrade, moving far from the high-symmetry configuration at $\alpha = 0$; this can be see in the Q factors obtained for mode 1 and mode 2 shown in panels (d) and (f), respectively. Here the scatter symbol size is directly proportional to the feature visibility, in such a way to elucidate the effect of OMS especially around normal incidence. Large Qs of about 1000 and 650 at $\alpha = 0$ respectively reduce to about 500 and 100 at large angles. Interestingly, mode 2 shows a more marked decrease, whereas mode 1 tends to a constant value in the investigated range. In the ideal metasurface simulations, the imaginary part of the simulated eigenfrequencies is exclusively due to the radiative loss channel; this results in a radiative Q factor, Q_r, diverging at normal incidence. For a more realistic comparison, we artificially include the effects of nonideal patterning by rescaling the simulated Q_r by an empirical factor $\alpha_{nr} = 20$. Moreover, we model the effect of different loss channels (roughness-induced scattering, surface state absorption, etc.) not included in the simulation by introducing an extra inner loss term, Q_m, which has been taken as $Q_m = 1100$ and $Q_m = 700$ for mode 1 and mode 2, respectively. The resulting total Q factor, which can be written as $Q_{\text{tot}}^{-1} = (Q_r/\alpha_{nr})^{-1} + Q_m^{-1}$, is reported in Figs. 4(e) and 4(g): the semiempirical estimation shows

good agreement with the outcome of experimental fits. For the sake of comparison, we analyzed the spectra measured in X-pol; while obtaining acceptable results for mode 2, the weaker mode 1 cannot be reliably fitted, especially in the region around $\alpha = 0$, where quasi-BICs show their most interesting regime. The full data analysis can be found in Appendix D. Note that, while U-pol and X-pol tilted spectroscopy are valid tools for identifying quasi-BICs at finite angles, both signals do not produce clear results when normal incidence is evaluated, which in our case is the most interesting point since it represents the condition closer to the pure BIC modes.

III. CONCLUSIONS

In this paper we have proposed and shown the application of a class of derivative spectroscopy—optomechanical modulation spectroscopy—that exploits a mechanical modulation to analyze weak or hidden spectral features. It enables the use of derivative spectroscopy through inner modulation and with cw single sources, enhancing selected features in multiresonance systems. Given the common nature of flexural, torsional, or breathing mechanical modes, OMS finds applications in a wide class of photonic devices, especially when undesirable background signals originating for the substrate-coupling scheme masks the resonances under investigation.

OMS has been validated by investigating an optomechanical BIC in a dielectric metasurface, which is a hybrid device experimentally characterized here. In perspective, such a platform can be an interesting avenue for dynamical control of narrow photonic features. On the one hand, the high Q factor could be used to exploit radiation pressure for optomechanical effects in metasurfaces and, more in general, in devices with delocalized photonic resonances where polarization effects can be better exploited [29]. On the other hand, the mechanical perturbation could be used to accurately control the BIC to quasi-BIC transition in future ultra-high-quality photonic devices, allowing working at normal incidence for applications in the guise of what is done with dark and bright excitons in light-matter systems [37].

ACKNOWLEDGMENTS

APPENDIX A: THEORETICAL CONSIDERATIONS

Optomechanical modulation spectroscopy is a technique based on optical transduction of mechanical motion, which is currently used to evaluate the coherently or thermally

excited motion in several class of optomechanical devices [12]. Let us suppose that we have an optical linear response signal at a frequency ω, $O(\omega)$; this can generally indicate transmission, reflection, etc. As routinely happens in several devices, $O(\omega)$ can originate from a resonant phonic system with complex eigenfrequency ω_0; in that case, the frequency dependence of $O(\omega)$ enters through a detuning term, $\Delta\omega = \omega - \omega_0$. When the signal interacts with a mechanical system it gains an extra, time-dependent term, $M(\Delta\omega)$:

$$O(\Delta\omega) = O_0(\Delta\omega) + M(\Delta\omega)\Delta x. \qquad (A1)$$

Here $O_0(\Delta\omega)$ is the static signal and Δx is a generalized mechanical displacement. With no loss of generality, we can restrict ourselves to a specific mechanical frequency, ω_m, in such a way that Δx is a harmonic function of ω_m and can be easily detected in an experimental setup by demodulating with a known reference signal at the same frequency. Considering usually small displacements, at the first order $M(\Delta\omega)$ can be expressed as

$$M(\Delta\omega) = \frac{\partial O(\Delta\omega)}{\partial x} = \frac{\partial O(\Delta\omega)}{\partial \omega_0}\frac{\partial \omega_0}{\partial x}, \qquad (A2)$$

where we have applied the chain rule for the derivatives. The last term in Eq. (A2) is the optomechanical coupling, $g_{OM} = \partial\omega_0/\partial x$ [12], which values the strength of optomechanical interaction. Exploiting the fact that the optical signal depends only on the detuning, we can apply a variable change and see that

$$\frac{\partial O(\Delta\omega)}{\partial \omega_0} = -\frac{\partial O(\Delta\omega)}{\partial \omega}. \qquad (A3)$$

The last term is the frequency derivative of the optical signal. Substituting Eq. (A3) into Eq. (A2) and integrating in $\delta\omega$, we obtain

$$\int M(\Delta\omega)d\omega = g_{OM}\int -\frac{\partial O(\Delta\omega)}{\partial \omega}d\omega = -g_{OM}O(\Delta\omega), \qquad (A4)$$

that is, the original signal scaled by the coupling constant with opposite sign, $-g_{OM}$. In a real experiment, the total reflectivity or transmissivity from a device can be made of the sum of different contributions; analyzing them using the OMS technique, each one will be subjected to an enhancement proportional to their own coupling constant. The model here described can be applied to resonant photonic systems, including the one described in the main text, manifesting in Lorentzian or Fano lineshapes and Fabry-Perot oscillations.
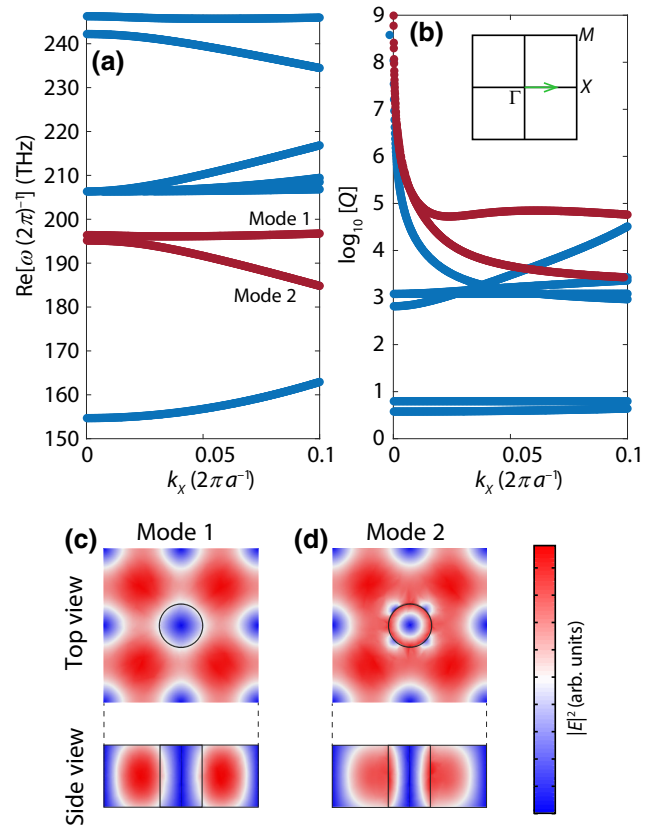

FIG. 5. (a) Band structure (left) and quality factor (right) for the infinite photonic crystal along the Γ-X high-symmetry path in the first Brillouin zone (inset). The modes under investigation have been indicated in red. Square modulus of the electric field for mode 1 (b) and mode 2 (c) at Γ.

APPENDIX B: SIMULATIONS

1. Metasurface design

BICs have been designed by considering a single, 220-nm-thick Si slab with a square lattice pattern of circular holes. Using a FEM solver, we simulate the optical band structure using Floquet-Bloch boundary conditions. We focus on two BICs closely spaced in frequency: the lattice constant and filling factor have been tuned to shift the two resonances within the laser operating range (1520–1570 nm). The final geometrical parameters of the unit cell are reported in Fig. 1 in the main text. Figure 5(a) shows the simulated band structure around 200 THz along a portion of the Γ-X high-symmetry path in the first Brillouin zone. In the right panel, we show the mode quality factors on a logarithmic scale for the very same eigenstates depicted in the left panel. As can be seen, few modes have a singular Q value at Γ, which is a signature of the BICs. The modes we investigate in the experiment are colored red for clarity.

Figure 5 also reports the simulated electric field norm in the proximity of Γ for both modes. As can be seen,
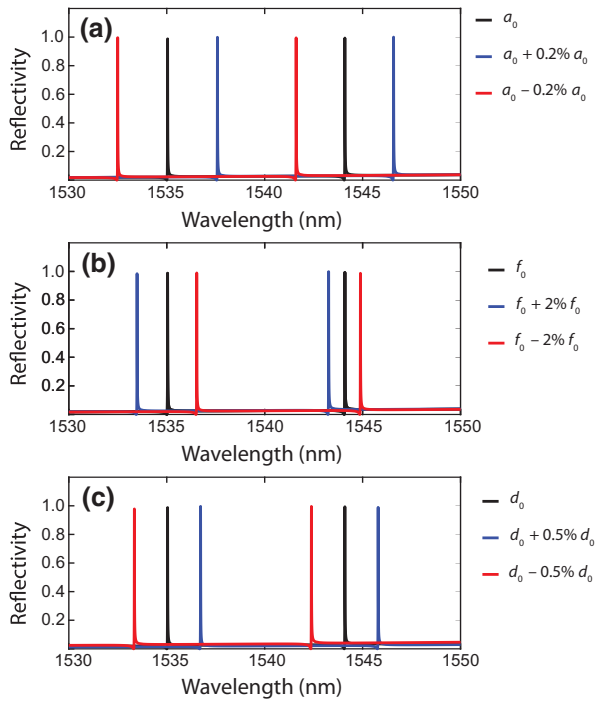
FIG. 6. Simulated reflectivity for small variations of the nominal device parameters in terms of the (a) lattice constant, (b) filling factor, and (c) device layer thickness.

the modal shape is quite similar, with a larger field confinement around the hole for mode 2 with respect to mode 1. This makes the former more sensitive to symmetry breaking induced by the nonperfect hole circularity, which translates to a larger signal in crosspolarization (X-pol). This is confirmed by the results shown in the main text, especially considering Fig. 2, where mode 1 does not show any contribution in the X-pol reflectivity signal. The dependence of the simulated spectra on the simulation parameters is reported in Fig. 6. Small variations of the lattice constant a [panel (a)], filling factor f [panel (b)], and device layer thickness d [panel (c)] with respect to the nominal final parameters a_0, f_0 and d_0 produce a rigid shift of the spectra without any significant change in their functional shape. In order to guarantee that at least a few of the fabricated devices will have quasi-BICs within the laser range, we fabricate device arrays where both the electron beam dose and lattice constant are varied. This produces the right parameter combination that provides features in the right spectral position.

2. Coupling constant estimate

The coupling constants reported in the main text have been obtained by performing simulations by means of the rigorous coupled wave analysis (RCWA) method, using the implementation in Ref. [32] that mostly relies on Ref. [38]. Here, in order to reduce the computational load,
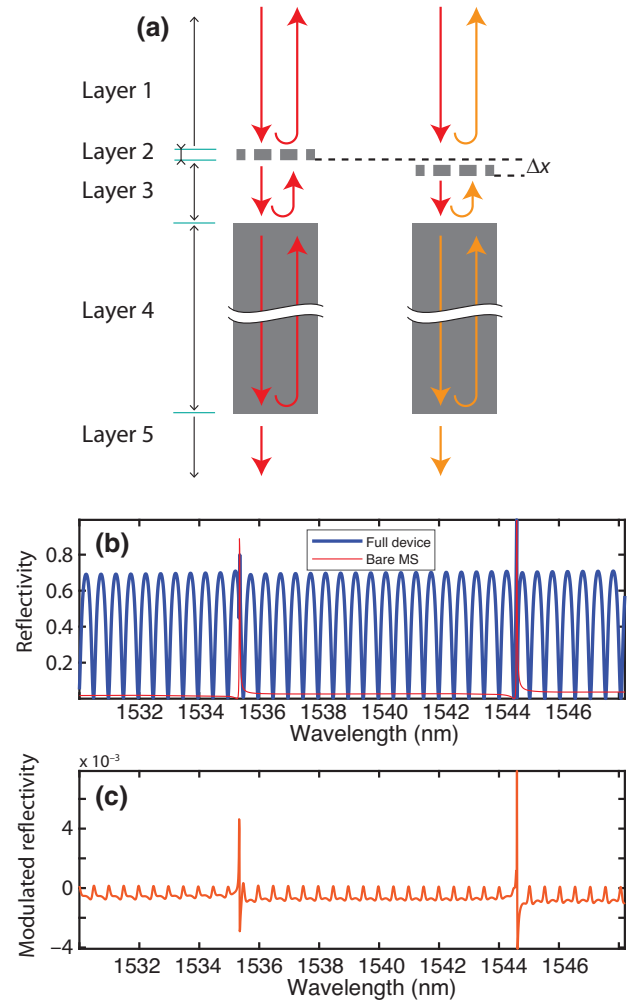

FIG. 7. (a) Sketch of mechanical action effects on the system resonances. (b) Infinite crystal reflectivity simulations at $\alpha = 1.5°$ by considering the full device (blue) and the bare metasurface contribution (red). (c) Simulated modulation spectrum.

we adopt a truncation scheme for the Fourier basis that is different for the various layers that constitute the structure. Specifically, the structure consists of five layers: *layer 1* (air superstrate), *layer 2* (patterned silicon membrane), *layer 3* (air spacer), *layer 4* (silicon handle wafer), *layer 5* (air substrate); see Fig. 7(a). We solve the Fourier modal equations over a basis consisting of 121 spatial harmonics (i.e., employing the square truncation scheme with 11×11 modes) in layers 1–3, and the Fourier modal equations over a basis consisting of a single spatial harmonic for layers 4–5. The scattering matrix propagation algorithm is adapted in order to properly keep into account the relevant harmonics at the transition between layers 3 and 4. This method eliminates the calculation of unnecessary diffracted waves in layers 4 and 5, while maintaining the correct description of the near field that exists in layers 1 and 3 close to the patterned silicon membrane. Mixed Fourier factorization rules [39] have not been employed.

The coupling constant estimate starts with assuming that the mechanical modes under investigation vary slowly with respect to the laser spot size, which has been estimated to be about 35 μm. In this regime, the mechanical action can be modeled by considering a static shift Δx of the device layer 2. As can be seen in the scheme of Fig. 7, this produces a change in layer 3 thickness, giving an extra phase shift to light, $\Delta\phi = \phi_0 + k \times \Delta x$, being ϕ_0 the phase gain by light traveling within layer 3 at rest position and k the wavevector. This extra, mechanics dependent term subsequently modifies all the next scattering events, ultimately resulting in the modulated reflectivity we measure in our experiment.

A typical, simulated static reflectivity spectrum at 1° light incidence is reported in Fig. 7(b). Here the isolated metasurface contribution to the full device spectrum has been additionally plotted in red. A simulated modulation spectra at the same incident angle is reported in panel (c). Note that the modulation is stronger in the spectral region with the quasi-BIC modes contribution. This is expected since the coupling constant is proportional to an overlap integral between mechanical and electromagnetic fields [40,41]. The modulated reflectivity signal is given by the product of the coupling constant g_{OM} and the derivative of the static optical response; the latter can be directly obtained from the results of panel (b), allowing the spectral evaluation of g_{OM}.

3. Considerations on feature contrast

From the experimental results of Fig. 4 in the main text, it is seen that the quasi-BIC features tend to disappear within the substrate signal as we move closer to normal incidence, corresponding to the condition with the largest radiative Q factors. This effect depends on the interplay between external and internal losses in the system, i.e., on the relative weight of scattering into the main external channels (reflection and transmission) and into spurious internal channels (dielectric absorption and roughness-induced scattering). A simple, physically insightful picture can be provided by the two-port coupled-mode theory (CMT) for photonic resonators. Relying on the theory exposed in Ref. [34], specialized here for the case of an isolated resonance and a symmetric system, we can write the reflection [$r(\omega)$] and transmission [$t(\omega)$] coefficients as

$$r(\omega) = \rho + \frac{i\gamma_e(\rho \pm i\tau)}{\omega - \omega_0 - i(\gamma_e + \gamma_i)},$$
$$t(\omega) = i\tau + \frac{i\gamma_e(\pm\rho + i\tau)}{\omega - \omega_0 - i(\gamma_e + \gamma_i)}, \qquad \text{(B1)}$$

where ω_0 is the resonance frequency, $\rho \in [0,1]$ is the off-resonance reflection coefficient, $\tau = \sqrt{1 - \rho^2}$, and γ_e (γ_i) is the external (internal) loss rate. Equations (B1) describe Fano resonances for both reflectance and transmittance
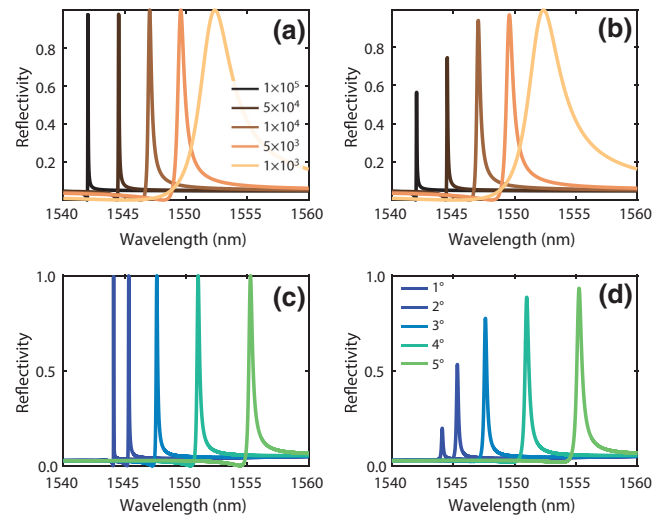

FIG. 8. Simulated reflectivity of a general two-port system by considering resonances with different radiative loss and (a) zero or (b) small nonradiative loss, respectively. Full PPML simulations of mode 2 of the isolated metasurface reproduce the expected behavior by considering a purely real silicon dielectric constant (c) and including a small residual material absorption (d).

spectra, as expected. Considering a series of resonances with increasing γ_e and with no internal loss ($\gamma_i = 0$), we obtain the reflectance features with unitary contrast shown in Fig. 8(a). Note that the resonant frequency in each case has been slightly shifted to improve the plot visibility. Including a small internal loss fixed for all the resonances [$\gamma_i = \omega_0/(3 \times 10^5)$], the situation dramatically changes and the resonances show a contrast decrease inversely proportional to their external loss rate; see Fig. 8(b). The simple CMT already catches the main features we have observed in the experiment. Full electromagnetic simulations based on RCWA [periodically patterned multi layer (PPML) [32]] for the bare metasurface infinitely extended in the *x-y* plane, as a function of incident angle, are reported in Fig. 8(c). Here we focus on mode 2 and consider a real dielectric constant for the material constituting the metasurface (Si $-$ $\varepsilon_{Si} = 12.2$). As expected, all the resonant features have the same contrast and show the familiar linewidth narrowing moving towards normal incidence. A different scenario can be found by just considering a complex dielectric constant with a very small imaginary part, $\varepsilon_{Si} = 12.2 + i0.001$. RCWA simulation reported in Fig. 8(d) confirms the trend expected from the CMT, further validating our experimental observations.

APPENDIX C: FABRICATION

The silicon metasurfaces are fabricated on standard silicon-on-insulator (SOI) samples with a top silicon layer thickness of 220 nm (resistivity about 1–10 W cm^{-1}, with

a lightly p-doping of 10^{15} cm^{-3}) and a buried oxide layer thickness of 2 μm and a bulk silicon handling support of 675 ± 25 μm. As the sample needs to be as thin as possible, we first lower the initial thickness of the sample, etching the Si from the backside with an isotropic Si recipe (SF6 only) with a STS AOE inductively coupled plasma (ICP) etcher. Around 150 μm of silicon is removed from the backside during this isotropic etching. After that, and to avoid light transmission leaks, a black silicon layer is created on the backside of the sample with the same ICP tool using a recipe based on a $SF_6 + O_2$ mixture gas. Process parameters as pressure (70 mT), bias voltage (15 W), gas ratios (1:2), and chuck temperature (0 °C) are adjusted to create the optimal conditions for the formation of black silicon. With this process, the formation of 500-nm-high black silicon needed an etching time of 15 min.

The fabrication of the BIC structures in the topside of the sample is based on an electron beam direct writing process performed on a 100 nm of polymethylmethacrylate (PMMA) positive resist. The mentioned electron beam exposure, performed with a Raith150 tool, is optimized to reach the required dimensions by employing an acceleration voltage of 10 KeV and an aperture size of 30 μm. After developing the PMMA resist using the MIBK/IPA developer, the resist patterns are transferred into the SOI samples by employing an optimized ICP-RIE process with fluoride gases. After removing the PMMA resist with an oxygen plasma (10 min), the silica BOX is removed under the BIC structures using a 50% hydrofluoric vapor bath for 5 min to ensure the complete etching of the 2 μm silica BOX.

APPENDIX D: EXPERIMENTAL CHARACTERIZATION

1. Piezoelectric actuator spectrum

The full lock-In amplitude (R_{LI}) spectrum of the piezoelectric actuator is reported in Fig. 9. The measurement, in vacuum condition (about 10^{-5} mbar), is performed by selecting a laser wavelength far from the quasi-BIC resonances and demodulating the reflectivity signal with the ac voltage fed to the piezo. As can be seen, the majority
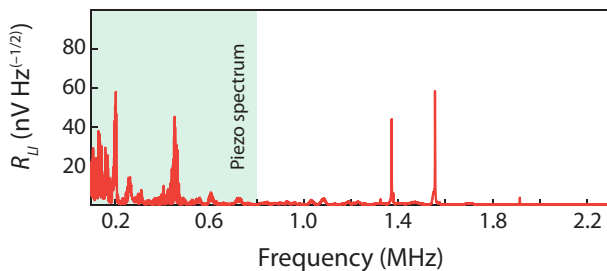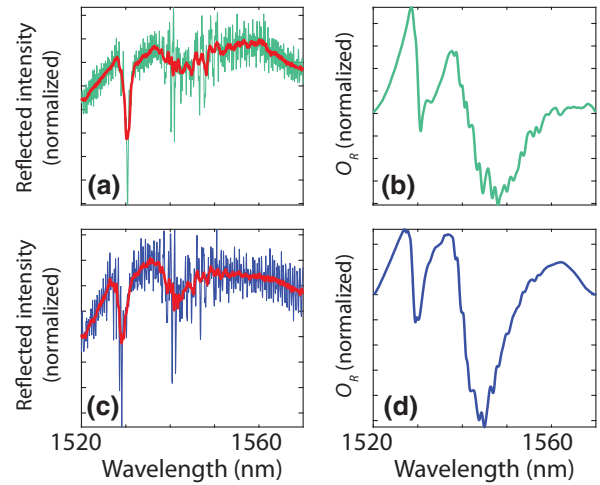

FIG. 10. Normalized U-pol and reconstructed spectra comparison. Signals at 4° (a),(b) and −4° (c),(d) incidence, respectively. The red line is a 20 points (out of 8697) moving average.

of piezo mechanical modes are localized below 1 MHz, while metasurface modes are visible, as narrow resonance, around 1.39, 1.57, and 1.9 MHz. The mode at 1.57 MHz is the one investigated in the main text.

2. Normalized spectra

In order to better appreciate the effect of OMS to large angles of incidence, it is significant to consider the normalized spectra for U-pol and the reconstructed ones, O_R, as shown in Fig. 4 in the main text. Figure 10 reports this comparison for two selected angles of incidence, $\alpha = \pm 4°$, respectively. The OMS gives an enhancement of the feature contrast [panels (b)–(d)] when compared to the U-pol signal [panels (a)–(c)]. Similar effects are present for all the measured angles of incidence. The decrease in the quality of the spectral features for the widest angles (for both signals) is not related to OMS but rather to the small numerical aperture of the focusing lens, which fails at efficiently collecting radiation at large angles.

3. Crosspolarization spectra analysis and the overall visibility ratio

As discussed in the main text, it is possible to enhance the feature visibilities by performing crosspolarization spectroscopy. The basic idea is that a particular geometry or simply geometrical imperfection in the metasurface pattern results in a sensitive polarization rotation, which is essentially negligible for light propagating in the homogeneous multilayers constituting the substrate. As shown in Fig. 2 in the main text, X-pol spectroscopy can indeed be used to increase the visibility of one of the two quasi-BICs under investigation (mode 2), while the polarization rotation of mode 1 is too weak to be exploited in the

FIG. 9. Broad mechanical spectrum. The piezo actuator modes are concentrated in the light green area.
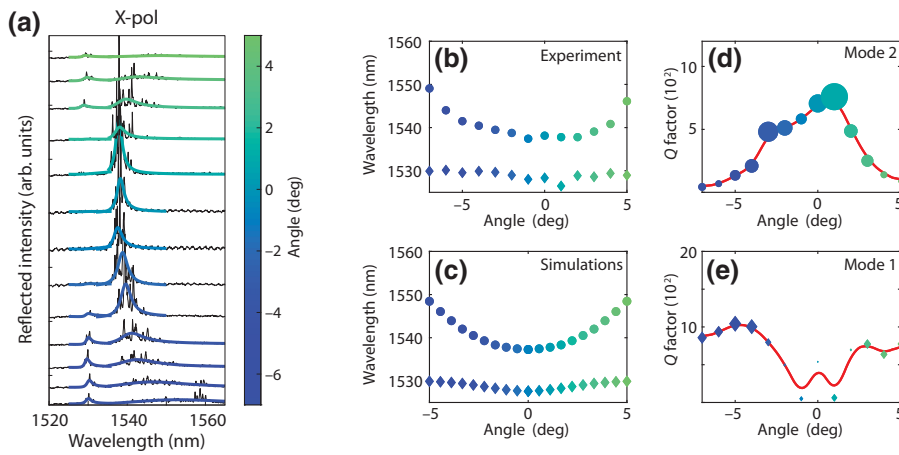
FIG. 11. (a) Waterfall plot of X-pol spectra at the metasurface center for different incident angles. Best fits with Fano lineshapes are indicated with bold, colored lines. (b),(c) Experimental and simulated frequency dispersions. Experimental (d) Q factors for mode 1 (d) and mode 2 (e) respectively. The scatter point size is proportional to the feature visibility; red lines are guides for the eyes.

same way. We attribute this difference to the field distributions of the two modes (see Fig. 5), which show a different degree of confinement around the pattern circular holes. Moreover, being the magnitude of the effect dependent on geometrical imperfections, the X-pol response is not homogeneous over the device, as reported in Fig. 2 in the main text. Despite the above limitations, we perform quasi-BIC spectroscopy using X-pol signals for a better comparison with the OMS introduced in our manuscript. Figure 11 summarizes the main results for spectra taken at the metasurface center position. As can be seen, the Fano fits shown in panel (a) are reliable enough to reproduce the expected frequency dispersion of the modes under investigation [see the experimental results in (b) and simulations in (c)]. A more complicated situation arises when considering the Q factors. Mode-2 analysis [see panel (d)] gives

same maximum Q as that obtained with OMS, although with a broader distribution, probably due to uncertainties in the linewidth determination due to the multiple substrate oscillations visible within the quasi-BIC bandwidth. The Q factors for mode 1 [panel (e)] are instead extremely unreliable, given by the poor visibility of the features close to normal incidence, which is here represented using a proportional scatter point size.

It can be interesting to perform an overall comparison of the different signals we have used to investigate the quasi-BICs. We define a visibility ratio by considering the ratio between the maxima peak to peak of the optical signal and of the background signal far from resonance. Figure 12 shows the visibility ratio for the different data as a function of the angle of incidence. As can be seen, a poor visibility ratio is found for the unfiltered polarization reflectivity (U-pol). X-pol spectra give a good visibility ratio for mode 2, while it is greatly reduced for mode 1, as described in the previous paragraph. Finally, reconstructed signals with OMS produce a large and reliable visibility ratio for both modes at all angles of incidence.
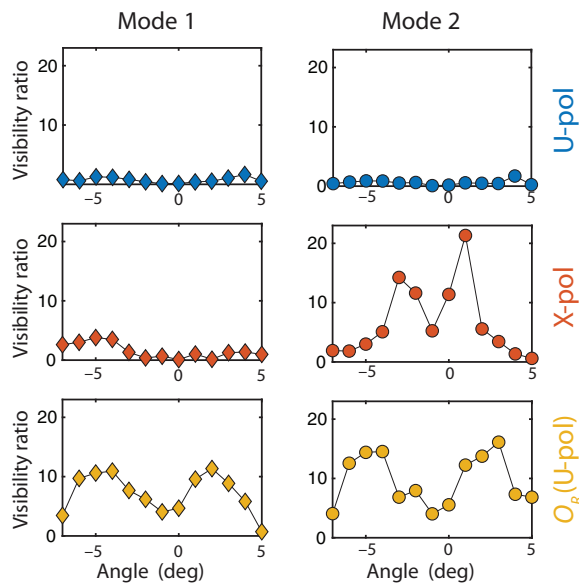

FIG. 12. Comparison of the visibility ratio for mode 1 (top row) and mode 2 (bottom row) for unfiltered, crosspolarized and OMS-reconstructed spectra, respectively.

[1] D. A. Skoog, F. J. Holler, and S. R. Crouch, *Principles of Instrumental Analysis* (Cencage, Boston, MA, 2017).
[2] P. Werle and F. Slemr, Signal-to-noise ration analysis in laser absorption sspectrometers using optical multipass cells, Appl. Opt. **30**, 430 (1991).
[3] D. S. Bomse, A. C. Stanton, and J. A. Silver, Frequency modulation and wavelength modulation spectroscopies: Comparison of experimental methods using a lead-salt diode laser, Appl. Opt. **31**, 718 (1991).
[4] R. M. Hexter, Excitation-modulation spectroscopy: A technique for obtaining vibrational spectra of excited electronic states, J. Opt. Soc. Am. **53**, 703 (1963).
[5] M. Cardona, Modulation spectroscopy of semiconductors, in *Festkörperprobleme 10. Advances in Solid State Physics*, Vol. 10, edited by O. Madelung (Springer, Berlin, 1970).
[6] K. Takagi, S. V. Nair, J. Saito, K. Seto, R. Watanabe, T. Kobayashi, and E. Tokunaga, Plasmon modulation

spectroscopy of noble metals to reveal the distribution of the fermi surface electrons in the conduction band, Appl. Sci. **7**, 1315 (2017).

[7] A. T. oczko, R. Oliva, T. Woźniak, J. Kopaczek, P. Scharoch, and R. Kudrawiec, Anisotropic optical properties of GeS investigated by optical absorption and photoreflectance, Mater. Adv. **1**, 1886 (2020).

[8] T. Liu, Y. Foo, J. A. Zapien, M. Li, and S.-W. Tsang, A generalized Stark effect electromodulation model for extracting excitonic properties in organic semiconductors, Nat. Commun. **10**, 5089 (2019).

[9] M. Caironi, M. Bird, D. Fazzi, Z. Chen, R. D. Pietro, C. Newman, A. Facchetti, and H. Sirringhaus, Very low degree of energetic disorder as the origin of high mobility in an *n*-channel polymer semiconductor, Adv. Funct. Mater. **21**, 3371 (2011).

[10] G. Vivó-Truyols, J. Torres-Lapasió, A. van Nederkassel, Y. V. Heyden, and D. Massart, Automatic program for peak detection and deconvolution of multi-overlapped chromatographic signals: Part I: Peak detection, J. Chromatogr. A **1096**, 133 (2005).

[11] T. C. O'Haver, A. F. Fell, G. Smith, P. Gans, J. Sneddon, L. Bezur, R. G. Michel, J. M. Ottaway, J. N. Miller, T. A. Ahmad, A. F. Fell, B. P. Chadburn, and C. T. Cottrell, Derivative spectroscopy and its applications in analysis, Anal. Proc. **19**, 22 (1982).

[12] M. Aspelmeyer, T. J. Kippenberg, and F. Marquardt, Cavity optomechanics, Rev. Mod. Phys. **86**, 1391 (2014).

[13] F. H. Stillinger and D. R. Herrick, Bound states in the continuum, Phys. Rev. A **11**, 446 (1975).

[14] C. W. Hsu, B. Zhen, A. D. Stone, J. D. Joannopoulos, and M. Soljačic, Bound states in the continuum, Nat. Rev. Mat. **1**, 16048 (2016).

[15] D. C. Marinica, A. G. Borisov, and S. V. Shabanov, Bound States in the Continuum in Photonics, Phys. Rev. Lett. **100**, 183902 (2008).

[16] Y. Plotnik, O. Peleg, F. Dreisow, M. Heinrich, S. Nolte, A. Szameit, and M. Segev, Experimental Observation of Optical Bound States in the Continuum, Phys. Rev. Lett. **107**, 183901 (2011).

[17] M. I. Molina, A. E. Miroshnichenko, and Y. S. Kivshar, Surface Bound States in the Continuum, Phys. Rev. Lett. **108**, 070401 (2012).

[18] C. W. Hsu, B. Zhen, J. Lee, S.-L. Chua, S. G. Johnson, J. D. Joannopoulos, and M. Soljačic, Observation of trapped light within the radiation continuum, Nature **499**, 188 (2013).

[19] C. W. Hsu, B. Zhen, S.-L. Chua, S. G. Johnson, J. D. Joannopoulos, and M. Soljačic, Bloch surface eigenstates within the radiation continuum, Light Sci. Appl. **2**, 84 (2013).

[20] B. Zhen, C. W. Hsu, L. Lu, A. D. Stone, and M. Soljačic, Topological Nature of Optical Bound States in the Continuum, Phys. Rev. Lett. **113**, 257401 (2014).

[21] H. M. Doeleman, A. A. Francesco Monticone, Wouter den Hollander, and A. F. Koenderink, Experimental observation of a polarization vortex at an optical bound state in the continuum, Nat. Photonics **12**, 397 (2018).

[22] Y. Akahane, T. Asano, B.-S. Song, and S. Noda, High-Q photonic nanocavity in a two-dimensional photonic crystal, Nature **425**, 944 (2003).

[23] K. Srinivasan, P. E. Barclay, M. Borselli, and O. Painter, Optical-fiber-based measurement of an ultrasmall volume high-Q photonic crystal microcavity, Phys. Rev. B **70**, 081306(R) (2004).

[24] D. K. Armani, T. J. Kippenberg, S. M. Spillane, and K. J. Vahala, Ultra-high-Q toroid microcavity on a chip, Nature **421**, 925 (2003).

[25] M. Galli, S. L. Portalupi, M. Belotti, L. C. Andreani, L. O'Faolain, and T. F. Krauss, Light scattering and Fano resonances in high-Q photonic crystal nanocavities, Appl. Phys. Lett. **94**, 071101 (2009).

[26] R. Leijssen and E. Verhagen, Strong optomechanical interactions in a sliced photonic crystal nanobeam, Sci. Rep. **5**, 15974 (2015).

[27] The vanishing intensity of the X-pol signal prevents its direct demodulation at the LIA, forcing the use of the stronger U-pol signal.

[28] L. Baldacci, A. Pitanti, L. Masini, A. Arcangeli, F. Colangelo, D. Navarro-Urrios, and A. Tredicucci, Thermal noise and optomechanical features in the emission of a membrane-coupled compound cavity laser diode, Sci. Rep. **6**, 31489 (2016).

[29] S. Zanotto, A. Tredicucci, D. Navarro-Urrios, M. Cecchini, G. Biasiol, D. Mencarelli, L. Pierantoni, and A. Pitanti, Optomechanics of chiral dielectric metasurfaces, Adv. Opt. Mater. **8**, 1901507 (2019).

[30] The Q factors are limited by molecular film damping, although their values do not directly impact the performance of OMS as long as the resonator is not overdamped (like at atmospheric pressure) and its spectral features can be clearly recognized.

[31] J. Gomis-Bresco, D. Navarro-Urrios, M. Oudich, S. El-Jallal, A. Griol, D. Puerto, E. Chavez, Y. Pennec, B. Djafari-Rouhani, F. Alzina, A. Martínez, and C. Sotomayor-Torres, A one-dimensional optomechanical crystal with a complete phononic band gap, Nat. Commun. **5**, 4452 (2014).

[32] Simone Zanotto PPML—periodically patterned multi layer, https://www.mathworks.com/matlabcentral/fileexchange/55401-ppml-periodically-patterned-multi-layer, 2021.

[33] For improved clarity of the waterfall plot, each curve has been offset by a factor $c \tan^{-1}(10\alpha)$, where c is a constant and α the angle of incidence.

[34] S. Zanotto, in *Fano Resonances in Optics and Microwaves*, edited by E. Kamenetskii, A. Sadreev, and A. Miroshnichenko (Springer, Berlin, 2018).

[35] S. Fan and J. Joannopoulos, Analysis of guided resonances in photonic crystal slabs, Phys. Rev. B **65**, 235112 (2002).

[36] S. Fan, W. Suh, and J. Joannopoulos, Temporal coupled-mode theory for the Fano resonance in optical resonators, J. Opt. Soc. Am. A **20**, 569 (2003).

[37] R. Ohta, H. Okamoto, T. Tawara, H. Gotoh, and H. Yamaguchi, Dynamic Control of the Coupling between Dark and Bright Excitons with Vibrational Strain, Phys. Rev. Lett. **120**, 267401 (2018).

[38] D. M. Whittaker and I. S. Culshaw, Scattering-matrix treatment of patterned multilayer photonic structures, Phys. Rev. B **60**, 2610 (1999).

[39] L. Li, New formulation of the Fourier modal method for crossed surface-relief gratings, J. Opt. Soc. Am. A **14**, 2758 (1997).

[40] S. G. Johnson, M. Ibanescu, M. A. Skorobogatiy, O. Weisberg, J. D. Joannopoulos, and Y. Fink, Perturbation theory for Maxwell's equations with shifting material boundaries, Phys. Rev. E **65**, 066611 (2002).

[41] A. G. Primo, N. C. Carvalho, C. M. Kersul, N. C. Frateschi, G. S. Wiederhecker, and T. P. Alegre, Quasinormal-Mode Perturbation Theory for Dissipative and Dispersive Optomechanics, Phys. Rev. Lett. **125**, 233601 (2020).